Correlated electronic structure of the kagome metal Mn_3Sn

Tianye Yu, Rui Liu, Yiran Peng, Pengyu Zheng, Guangwei Wang, Xiaobo Ma, Zhihong Yuan, and Zhiping Yin*
Department of Physics and Center for Advanced Quantum Studies, Beijing Normal University, Beijing 100875, China

(Received 1 August 2022; revised 18 October 2022; accepted 19 October 2022; published 1 November 2022)

Mn_3Sn is a fascinating kagome metal exhibiting anomalous Hall effect, spin Hall effect, and anomalous Nernst effect. Using density functional theory plus dynamical mean-field theory (DFT + DMFT), we investigate the electronic structures of Mn_3Sn in the paramagnetic and noncollinear antiferromagnetic (NAFM) states. In the paramagnetic state, Mn_3Sn has intermediate electronic correlation strength and exhibits typical features of kagome metals including flat bands, Dirac points, and saddle points. In the NAFM state, DFT + DMFT calculations reproduce well the experimental Mn magnetic moment and angle-resolved photoemission spectroscopy measurements. Electronic correlation shifts the bands around E_F and moves the Weyl point between K and M points from ~ 40 meV above E_F in DFT calculations to ~ 5 meV below E_F, which can strongly enhance the anomalous Hall effect and chiral anomaly observed in Mn_3Sn. More importantly, we find that the existence of the Weyl point along the K-M path depends strongly on the ordering pattern of the Mn moments in the NAFM state, which implies that the exotic properties arising from the Weyl points in Mn_3Sn can be manipulated by tuning the ordering pattern of the Mn moments in the NAFM state.

DOI: 10.1103/PhysRevB.106.205103

I. INTRODUCTION

Recently, kagome-lattice materials have attracted a great deal of attention because of the close relationship between their electronic band structures and topological states with novel topological excitations [1–3]. Theoretically, the band structure of kagome lattice hosts both flat bands which can be characterized by a Chern number [1,4,5] and linearly dispersive bands which may result in novel transport properties when the Fermi energy (E_F) is adjusted properly [6–9]. In recent years, flat bands (FBs), Weyl points (WPs), or Dirac points (DPs) are discovered in realistic kagome materials including ferromagnetic $Co_3Sn_2S_2$ [10–14], YMn_6Sn_6 [15], and Fe_3Sn_2 [5,16,17], antiferromagnetic FeSn [18,19], and paramagnetic CoSn [20,21].

Different from the paramagnetic or collinear (anti)ferromagnetic state shown in other kagome-lattice metals, Mn_3Sn has a noncollinear antiferromagnetic (NAFM) ground state at room temperature and exhibits a large anomalous Hall effect (AHE) [22], which can be understood in terms of Berry phase [23]. In addition to the AHE, some other novel phenomena including magnetic and magnetic inverse spin Hall effects [24], anomalous Nernst effect [25], and magneto-optical Kerr effect [26] have also been observed at room temperature. Moreover, experimental observations of the coexistence of chiral anomaly and AHE indicate the presence of Weyl points in this material [27], which has also been proposed by theoretical calculations [27,28]. The NAFM order plays an important role to understand these observations. We notice that the magnetic order of Mn_3Sn is complicated [29] and sensitive to the variation of composition, synthesis conditions [30,31], and temperature [32–34]. In this work, we focus on Mn_3Sn in the NAFM state which shows the above phenomena, with a Néel temperature of 430 K [22]. In the NAFM state, Mn atoms possessing a magnetic moment of $3.00\mu_B$ form an inverse triangular spin configuration [34,35]. The canting of two spins among three in the same layer towards the local easy axis leads to weak ferromagnetic moment of the order of approximately 0.005–$0.009\mu_B$ per unit cell [36,37]. Consequently, the magnetic configuration can be switched by an external magnetic field [22].

Besides the magnetism, electronic correlation effects have also been proved to be prominent due to the Mn $3d$ electrons. Kuroda *et al.* [27] carried out angle-resolved photoemission spectroscopy (ARPES) experiment and found that the band structure obtained by density functional theory (DFT) needs to be renormalized by a factor of ~ 5 in order to fit their experimental ARPES spectra, manifesting strong electronic correlation strength in this material. Using *ab initio* calculations, Zhang *et al.* [38] obtained the AHE conductivity of several antiferromagnetic compounds Mn_3X (X = Ge, Sn, Ga, Ir, Rh, and Pt) and drew a conclusion that the magnitude of AHE conductivity of these compounds does not follow the same trend as the spin-orbit coupling (SOC) magnitude of atom X, but is sensitive to the band structure and band filling. However, electronic correlation was not explicitly included in their calculations. In light of these reports, it is important to uncover the correlation effects on the electronic structure of Mn_3Sn. What is more, recent studies on a semimetal $YbMnSb_2$ illustrate that different magnetic configurations give rise to different topological states including Weyl nodes [39], a nodal line [40], and a gapped Dirac point [41]. Therefore, exploring how magnetic configuration influences electronic structure of Mn_3Sn is interesting.

*yinzhiping@bnu.edu.cn

In this paper, we employed state-of-the-art DFT plus dynamical mean-field theory (DFT + DMFT) method to uncover how electronic correlation effects modify the electronic structure of Mn_3Sn in the paramagnetic and NAFM states. Both the calculated averaged mass enhancement of Mn 3*d* electrons and bandwidth renormalization factor indicate that paramagnetic Mn_3Sn is an intermediately correlated kagome metal. Our DFT + DMFT results agree well with available experimental measurements in the NAFM state and present substantial band shifts relative to E_F and significant nonuniform bandwidth renormalizations for different bands. Electronic correlation moves the Weyl point between *K* and *M* points much closer to the Fermi level, which can boost the anomalous Hall effect and chiral anomaly observed in Mn_3Sn. Moreover, we investigated the effects of different magnetic orders on the electronic structures and topological properties and found that the existence of Weyl points along the *K*-*M* path depends strongly on the ordering pattern of the Mn moments. Therefore, the exotic properties due to the existence of the Weyl points in Mn_3Sn can be tuned by applying external magnetic field in the NAFM state.

II. METHODS AND STRUCTURAL DETAILS

We perform fully charge self-consistent DFT + DMFT calculations using the eDMFT code [42] developed by Haule *et al.*, where the DFT part is based on the linearized augmented plane-wave method as implemented in WIEN2K package [43]. The Perdew-Burke-Ernzerhof generalized gradient approximation [44] is used for the exchange-correlation functional. Brillouin-zone integrations are performed on a $20 \times 20 \times 22$ mesh. The atomic spheres R_{MT} are 2.50 Bohr for both Mn and Sn, and the plane-wave cutoff $K_{\max}$ is given by $R_{\mathrm{MT}}K_{\max} = 7.0$. The projector to local Green's function used in the DMFT part is fixed to the solution of the Dirac equation on the DFT level. In the DFT + DMFT calculations, we consider hybridization functions with an energy window of 20 eV (from −10 to 10 eV) around the Fermi level. The formula $U(n-1/2) - J\ (n-1)/2$ (n is the nominal occupation of Mn 3*d* electrons) is used to subtract the double counting. Coulomb interaction parameter $U = 4.0$ eV and Hund's exchange parameter $J_H = 0.45$ eV are used in our calculations, which describe experimental measurements [27] including the Mn magnetic moment and ARPES spectra well. All five Mn 3*d* orbitals are treated correlated and the rotationally invariant form of the local on-site Coulomb interaction Hamiltonian is applied. The DMFT quantum impurity problem is solved by continuous time quantum Monte Carlo method [45,46] at temperature $T = 116$ K. The spin-polarized calculations at the DFT level are also performed using the Vienna *Ab initio* Simulation Package (VASP) [47]. SOC is included in all the calculations.

Mn_3Sn has a hexagonal layered crystal structure with an *AB* stacking sequence crystallizing in the $P6_3/mmc$ space group (No. 194). We show the crystal structure and the first Brillouin zone of Mn_3Sn in Figs. 1(a) and 1(b), respectively. In each layer, Mn atoms form a kagome-type lattice consisting of triangles and slightly distorted hexagons; Sn atoms locate at the center of the hexagons. In our calculations, the experimentally determined atomic positions and lattice constants of

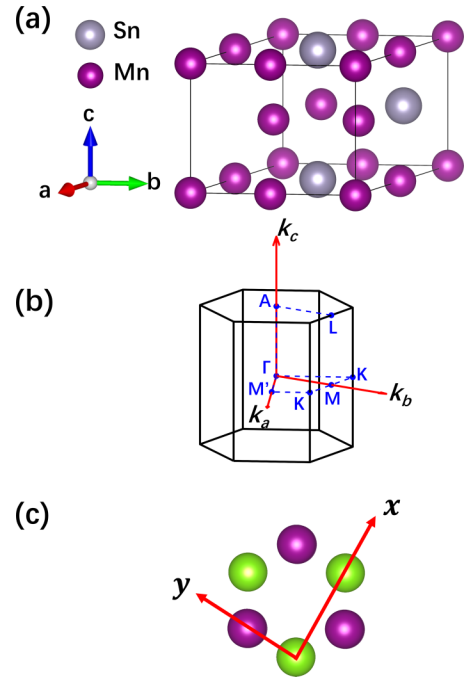

FIG. 1. (a) Crystal structure of Mn_3Sn with space group $P6_3/mmc$ (No. 194). (b) First Brillouin zone of Mn_3Sn. High-symmetry points for the band structure plots are depicted. (c) Top view along the *c* axis of Mn sublattice; purple and green balls represent Mn atoms in different layers. Local axes (x, y) are depicted; z axis points out of plane.

$a = 5.665$ Å, and $c = 4.531$ Å [34] are used. The local coordinate system of Mn used in calculations is shown in Fig. 1(c). Figure 2 presents several magnetic configurations which were put forward by Brown *et al.* [34] to fit experimental data, where Figs. 2(c) and 2(f) were considered to be the most possible configurations. When not indicated explicitly, our

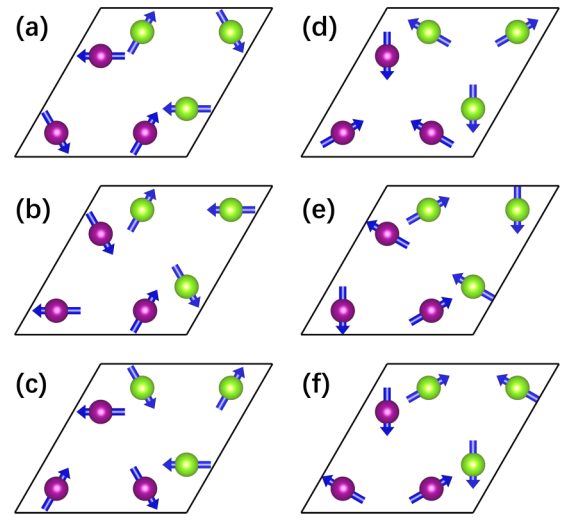

FIG. 2. (a)–(f) Possible magnetic configurations proposed in Ref. [34] to fit the results obtained by generalized neutron polarization analysis. Configurations (c) and (f) are the most likely, and have no difference in fitting the experimental results. Purple and green balls represent Mn atoms in different layers; blue arrows represent the directions of magnetic moments of Mn atoms.

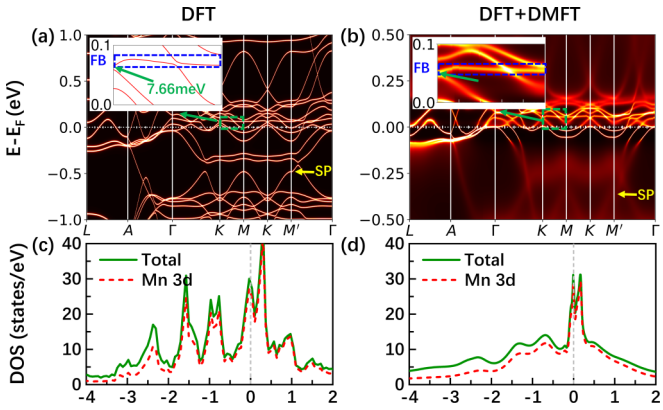

FIG. 3. (a) Band structure obtained by DFT in the nonmagnetic state. saddle point (SP) at M' is indicated by the yellow arrow. Inset: enlarged view of the flat band (FB) along K-M and the band gap induced by SOC at the Dirac point at K. (b) momentum-resolved spectral functions obtained by DFT + DMFT in the paramagnetic state. (c) and (d) are the momentum-integrated spectral functions (usually called density of states) corresponding to (a) and (b), respectively.

discussions on the noncollinear antiferromagnetic state are based on the results using the magnetic configuration shown in Fig. 2(c), which is consistent with Ref. [27].

III. RESULTS AND DISCUSSION

A. Correlated electronic structure in the paramagnetic state

We start with describing the electronic structure of Mn_3Sn in the paramagnetic state. Figure 3(a) presents the band structure obtained by DFT, presenting several features of an ideal kagome metal. Specifically, there is a FB along K-M near E_F ($\sim$ 80 meV above E_F). An electron-like band with its bottom slightly lower than E_F at M crosses the FB and forms a DP along the K-M path [48]. However, as shown in the inset of Fig. 3(a), this Dirac point is gapped by SOC. SOC also produces an energy gap of 7.66 meV at the Dirac point at K. Both FB and gapped DPs were also found in paramagnetic kagome metal CoSn [20,21]. In addition, we notice a saddle point (SP) at M' ($\sim$ 0.5 eV below E_F) which was also observed in ferromagnetic YMn_6Sn_6 [15]. The positions of FB, SP, and DP are also indicated in the spectral functions obtained by DFT + DMFT in Fig. 3(b). Notice that owing to the high Néel temperature of 430 K of Mn_3Sn, it is challenging to experimentally identify these typical features in the electronic structures of kagome metals in the paramagnetic state. Since the spectral functions usually have strong incoherent nature at high temperature, some bands will fade out in ARPES spectra, as reported for other correlated metals [49,50].

Next, we discuss electronic correlation effects in the paramagnetic state of Mn_3Sn. Figure 3(b) presents the spectral functions obtained by DFT + DMFT. At first glance, the spectra far from E_F are blurry, which means that the Mn 3d electrons are in incoherent states. Besides the incoherent feature caused by electronic correlation effects, we also find that the bands in the vicinity of E_F are moderately renormalized as compared to those obtained by DFT. For instance, noticing that the energy range in Fig. 3(a) is twice as large as that in Fig. 3(b), the band in Fig. 3(b) crossing E_F along L-A is compressed about twice as compared to the corresponding one in Fig. 3(a), suggesting the importance of electronic correlation effects. In addition to the bandwidth renormalization, the mass enhancement m^*/m_{DFT} at the Fermi energy can also quantify the strength of electronic correlation. Mn 3d yz electron with the smallest occupancy number of 1.06 is the most strongly correlated with $m^*/m_{\mathrm{DFT}} \approx 2.2$. On the other hand, Mn 3d z^2 electron with the largest occupancy number of 1.09 is the least correlated with $m^*/m_{\mathrm{DFT}} \approx 1.7$. The averaged mass enhancement of the Mn 3d electrons is $\sim$ 1.9. Based on the calculated averaged mass enhancement and bandwidth renormalization factor, we conclude that paramagnetic Mn_3Sn is an intermediately correlated kagome metal. Figures 3(c) and 3(d) present the momentum-integrated spectral functions (usually called density of states) corresponding to Figs. 3(a) and 3(b), respectively, showing an important feature of the Mn 3d partial momentum-integrated spectral functions which possess two sharp peaks near E_F. In the meantime, the total momentum-integrated spectral functions are mainly contributed by the Mn 3d partial momentum-integrated spectral functions in the whole energy range that we show. Compared with Fig. 3(c), electronic correlation effects flatten the momentum-integrated spectral functions far from E_F in Fig. 3(d), in accordance with the incoherent feature of the spectral functions far from E_F shown in Fig. 3(b), and narrow the two sharp peaks near E_F.

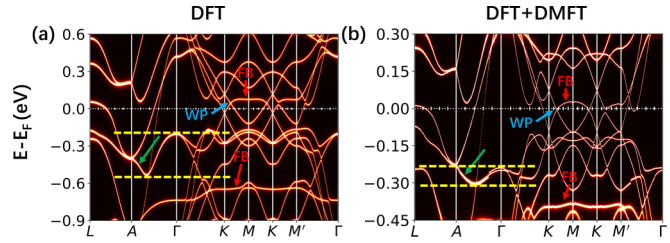

FIG. 4. (a) Band structure in the NAFM state obtained by DFT. FB and WP along K-M are indicated by the red and blue arrow, respectively. Green arrow indicates the band whose bandwidth is severely compressed along A-Γ in DFT + DMFT. Dashed yellow lines indicate the positions of the energy maximum and minimum of the severely compressed band along A-Γ. (b) Momentum-resolved spectral functions in the NAFM state obtained by DFT + DMFT.

B. Correlation effects in the noncollinear antiferromagnetic state

Figure 4(a) presents the DFT calculated band structure in the NAFM state, which is consistent with previous calculation [27]. We show the positions of both FB and WP in Figs. 4(a) and 4(b). In comparison with the paramagnetic state, the spectral functions shown in Fig. 4(b) obtained by DFT + DMFT have a wider coherent energy region, this is because the onset of magnetic order suppresses the magnetic fluctuations and the associated many-body renormalizations (quasiparticle mass enhancement). The mass enhancements of all five Mn 3d orbitals become comparable to each other with values in the range of 1.2 to 1.3. Intriguingly, while the calculated mass enhancement of each orbital is smaller, we find substantial bandwidth renormalizations for certain bands with respect to the DFT results. For example, the band crossing

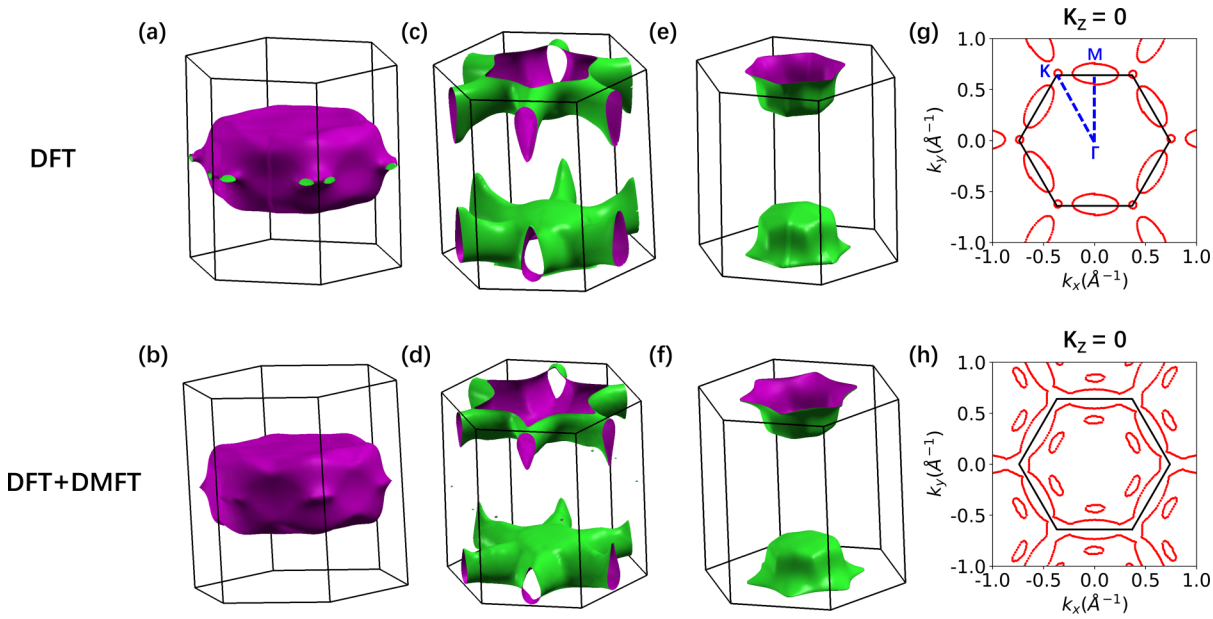

FIG. 5. Three-dimensional Fermi surfaces (a)–(f) of individual bands crossing the Fermi level and two-dimensional merged Fermi surfaces on the $k_z = 0$ plane (g), (h) of Mn_3Sn in the noncollinear antiferromagnetic state obtained by DFT (top row) and DFT + DMFT (bottom row) calculations.

E_F along L-A is compressed about twice. What is more, the bandwidth of the band along A-Γ indicated by the green arrow is compressed by a factor of almost 5. The large variation in bandwidth renormalization factor for different bands in the NAFM state suggests that it is inappropriate to compress the whole DFT bands by a single factor.

In addition to bandwidth renormalization, electronic correlation lowers the bands near E_F and changes the shape of Fermi surface, as shown in Fig. 5. In Fig. 4(a), we observe that one electron-like band crossing E_F along L-A-Γ forms an electron pocket around A [Fig. 5(c)]; one more strongly dispersive band crossing E_F along A-Γ also produces an electron pocket around A [Fig. 5(e)]. On the $k_z = 0$ plane, several bands cross E_F along the path Γ-K-M-K-M'-Γ and form one small electron pocket around K and a larger electron pocket around M and M' [Figs. 5(a) and 5(g)]. As shown in Fig. 4(b), after considering the electronic correlation effects of Mn 3d electrons, the bands near E_F are shifted downward, which increases the size of Fermi surface, such as the electron pocket around K. In the meantime, one small electron pocket is added along M'-Γ [Figs. 5(g) and 5(h)].

Previous experimental observations including the large AHE [22], anomalous Nernst effect [25], and chiral anomaly [27] support the existence of Weyl point near E_F. Several Weyl points have been theoretically found and characterized through its topological properties [28,38,51]. Besides, Kuroda *et al.* [27] pointed out that the Weyl point, as indicated by the blue arrow in Fig. 4(a), locating along the K-M path, is the most relevant for transport and other macroscopic measurements because it is closest to E_F. Comparing Figs. 4(a) and 4(b), we find that correlated effects shift the Weyl point from ∼ 40 meV above E_F to ∼ −5 meV below E_F which may have strongly enhanced the AHE, anomalous Nernst effect, and chiral anomaly. It is interesting to do high-resolution ARPES measurement to confirm the exact location of the Weyl point.

C. Comparison between the calculated and experimental measurements

In Fig. 6(a), we overlay our DFT and DFT + DMFT calculated band structures with experimentally determined ARPES spectra [27] along M-K-Γ. The DFT and DFT + DMFT results are presented by dotted and solid lines, respectively. We find that without considering extra bandwidth renormalization, the agreement between ARPES measurements and DFT + DMFT calculated bands is good enough, with the calculated E_F shifted downwards ∼ 80 meV. In particular, the intensity around K near E_F and along K-Γ in a large energy range are captured by the DFT + DMFT calculations. In contrast, with the DFT bands shifted upwards ∼ 10 meV to fit the experimental intensity at K, there are no DFT bands corresponding to experimental intensity along K-Γ below E_F. We further show the comparison between the DFT + DMFT

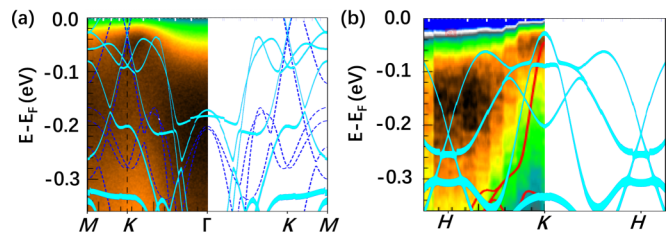

FIG. 6. Comparison among DFT + DMFT calculated momentum-resolved spectral functions (solid cyan lines), DFT calculated band structure (dashed blue lines), and ARPES measurements [27] along (a) M-K-Γ and (b) H-K in the NAFM state. Red line in (b) is the DFT band given by Ref [27]. E_F calculated by DFT + DMFT has been shifted downwards ∼ 80 meV to match the experiment value E_{exp} in (a) and (b); E_F calculated by DFT has been shifted upwards ∼ 10 meV to fit the experimental intensity at K in (a).

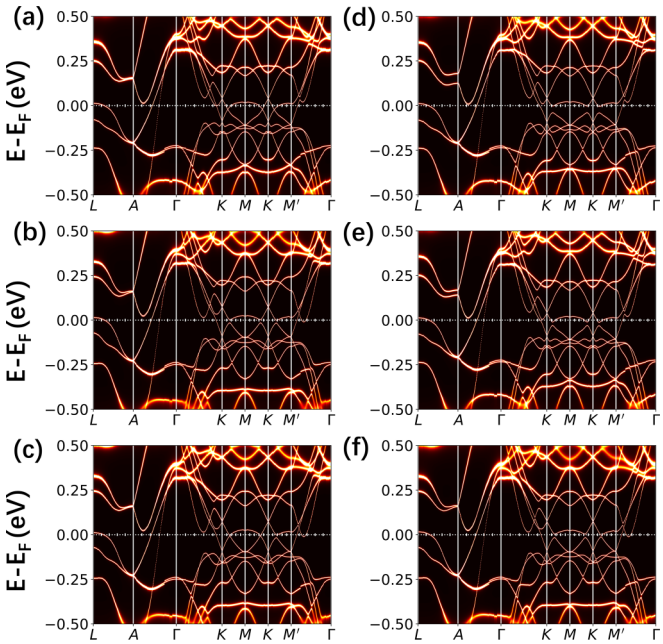

FIG. 7. DFT + DMFT calculated momentum-resolved spectral functions in various NAFM states corresponding to the magnetic configurations shown in Fig. 2.

calculated (solid cyan lines) and experimentally determined ARPES [27] along H-K in Fig. 6(b). The red lines are the DFT bands from Ref. [27]. It is evident that the DFT + DMFT results agree well with the experimental ARPES, whereas the DFT bands show large discrepancy with the experimental ARPES. In addition to the good agreement of the DFT + DMFT calculated spectral functions and experimental ARPES spectra, the DFT + DMFT calculated magnetic moment of Mn in the NAFM state is the same as experimental value of $\sim 3.00\ \mu_B$ [34], whereas the corresponding DFT calculated value is 3.13 μ_B.

D. Impact of magnetic configurations on the topological properties

Physical phenomena such as AHE and chiral anomaly in Mn_3Sn are observed in the NAFM state. In Fig. 2, we show several NAFM configurations which were previously proposed to compare with the results obtained by generalized neutron analysis [34]. These different magnetic-ordering patterns of the Mn moments exhibit many similarities in magnetic properties and electronic structures. For example, the DFT + DMFT calculated magnetic moments of Mn atoms of the six magnetic configurations are all the same and equal to 3.00 μ_B per Mn. To gain further insights into the low-energy physics of Mn_3Sn with different magnetic configurations, we present their corresponding spectral functions near E_F in Fig. 7. These spectral functions have several similarities and differences. To be specific, they all show significant coherence within the energy range that we show, and share similar shape of energy bands. But, there are still some differences in the details, such as whether there are gaps or not between bands. For instance, the two bands above E_F along L-A are degenerate at A except in Figs. 7(d) and 7(e). More importantly, the Weyl point along the K-M path near E_F is present only in Figs. 7(a) and 7(c), whereas in other cases a gap is opened at the corresponding Weyl point with the largest gap in Fig. 7(d). As is well known, the existence of Weyl points leads to Fermi-arc type surface states and other novel properties. Consequently, these differences demonstrate that the band topology and topological properties of Mn_3Sn are highly sensitive to the magnetic configuration of the Mn moments. Therefore, our results show that we can manipulate the existence of Weyl points and related properties such as AHE, negative magnetoconductance, and chiral anomaly by tuning the magnetic fields applied to this material.

IV. CONCLUSIONS

In summary, we demonstrate that paramagnetic Mn_3Sn exhibits typical features of kagome metals including flat bands, Dirac points, and saddle points. Mn 3d orbitals have intermediate electronic correlation strength. In the NAFM state, the DFT + DMFT calculated Mn magnetic moment and momentum-resolved spectral functions agree well with experimental measurements. Electronic correlation lowers the bands near E_F and moves the Weyl point along the K-M path from ~ 40 meV above E_F in DFT calculations to ~ 5 meV below E_F. The closeness of the Weyl point to the Fermi level can have a big impact on the AHE and chiral anomaly observed in Mn_3Sn [27]. More importantly, we find that the existence of the Weyl points between K and M points depends strongly on the ordering pattern of the Mn moments in the NAFM state. It indicates that the exotic properties connected to the Weyl points, including the AHE and chiral anomaly in Mn_3Sn, can be manipulated by tuning the ordering pattern of the Mn moments in the NAFM state.

ACKNOWLEDGMENTS

This work was supported by the National Natural Science Foundation of China (Grants No. 12074041 and No. 11674030), the Foundation of the National Key Laboratory of Shock Wave and Detonation Physics (Grant No. 6142A03191005), and the start-up funding of Beijing Normal University. The calculations were carried out using the high-performance computing cluster of Beijing Normal University in Zhuhai.

[1] Z. Liu, F. Liu, and Y. S. Wu, Chin. Phys. B **23**, 077308 (2014).
[2] A. Mielke, J. Phys. A **25**, 4335 (1992).
[3] K. Ohgushi, S. Murakami, and N. Nagaosa, Phys. Rev. B **62**, R6065(R) (2000).
[4] D. J. Thouless, M. Kohmoto, M. P. Nightingale, and M. den Nijs, Phys. Rev. Lett. **49**, 405 (1982).
[5] L. Ye, M. Kang, J. Liu, F. von Cube, C. R. Wicker, T. Suzuki, C. Jozwiak, A. Bostwick, E. Rotenberg, D. C. Bell, L. Fu,

R. Comin, and J. G. Checkelsky, Nature (London) **555**, 638 (2018).
[6] M. Z. Hasan and C. L. Kane, Rev. Mod. Phys. **82**, 3045 (2010).
[7] R. Yu, Z. Fang, X. Dai, and H. Weng, Front. Phys. **12**, 127202 (2017).
[8] X.-L. Qi and S.-C. Zhang, Rev. Mod. Phys. **83**, 1057 (2011).
[9] N. J. Ghimire and I. I. Mazin, Nat. Mater. **19**, 137 (2020).
[10] N. Morali, R. Batabyal, P. K. Nag, E. K. Liu, Q. N. Xu, Y. Sun, B. H. Yan, C. Felser, N. Avraham, and H. Beidenkopf, Science **365**, 1286 (2019).
[11] D. F. Liu, A. J. Liang, E. K. Liu, Q. N. Xu, Y. W. Li, C. Chen, D. Pei, W. J. Shi, S. K. Mo, P. Dudin, T. Kim, C. Cacho, G. Li, Y. Sun, L. X. Yang, Z. K. Liu, S. S. P. Parkin, C. Felser, and Y. L. Chen, Science **365**, 1282 (2019).
[12] L. Jiao, Q. Xu, Y. Cheon, Y. Sun, C. Felser, E. Liu, and S. Wirth, Phys. Rev. B **99**, 245158 (2019).
[13] J. X. Yin, S. S. Zhang, G. Q. Chang, Q. Wang, S. S. Tsirkin, Z. Guguchia, B. Lian, H. B. Zhou, K. Jiang, I. Belopolski, N. Shumiya, D. Multer, M. Litskevich, T. A. Cochran, H. Lin, Z. Q. Wang, T. Neupert, S. Jia, H. C. Lei, and M. Z. Hasan, Nat. Phys. **15**, 443 (2019).
[14] Q. Wang, Y. Xu, R. Lou, Z. Liu, M. Li, Y. Huang, D. Shen, H. Weng, S. Wang, and H. Lei, Nat. Commun. **9**, 3681 (2018).
[15] M. Li, Q. Wang, G. Wang, Z. Yuan, W. Song, R. Lou, Z. K. Liu, Y. Huang, Z. Liu, H. Lei, Z. Yin, and S. Wang, Nat. Commun. **12**, 3129 (2021).
[16] Z. Lin, J.-H. Choi, Q. Zhang, W. Qin, S. Yi, P. Wang, L. Li, Y. Wang, H. Zhang, Z. Sun, L. Wei, S. Zhang, T. Guo, Q. Lu, J.-H. Cho, C. Zeng, and Z. Zhang, Phys. Rev. Lett. **121**, 096401 (2018).
[17] J.-X. Yin, S. S. Zhang, H. Li, K. Jiang, G. Chang, B. Zhang, B. Lian, C. Xiang, I. Belopolski, H. Zheng, T. A. Cochran, S.-Y. Xu, G. Bian, K. Liu, T.-R. Chang, H. Lin, Z.-Y. Lu, Z. Wang, S. Jia, W. Wang, and M. Z. Hasan, Nature (London) **562**, 91 (2018).
[18] Z. Lin, C. Wang, P. Wang, S. Yi, L. Li, Q. Zhang, Y. Wang, Z. Wang, H. Huang, Y. Sun, Y. Huang, D. Shen, D. Feng, Z. Sun, J.-H. Cho, C. Zeng, and Z. Zhang, Phys. Rev. B **102**, 155103 (2020).
[19] M. Kang, L. Ye, S. Fang, J.-S. You, A. Levitan, M. Han, J. I. Facio, C. Jozwiak, A. Bostwick, E. Rotenberg, M. K. Chan, R. D. McDonald, D. Graf, K. Kaznatcheev, E. Vescovo, D. C. Bell, E. Kaxiras, J. van den Brink, M. Richter, M. P. Ghimire, J. G. Checkelsky, and R. Comin, Nat. Mater. **19**, 163 (2019).
[20] M. Kang, S. Fang, L. Ye, H. C. Po, J. Denlinger, C. Jozwiak, A. Bostwick, E. Rotenberg, E. Kaxiras, J. G. Checkelsky, and R. Comin, Nat. Commun. **11**, 4004 (2020).
[21] Z. Liu, M. Li, Q. Wang, G. Wang, C. H. P. Wen, K. Jiang, X. Lu, S. Yan, Y. Huang, D. Shen, J. Yin, Z. Wang, Z. Yin, H. Lei, and S. Wang, Nat. Commun. **11**, 4002 (2020).
[22] S. Nakatsuji, N. Kiyohara, and T. Higo, Nature (London) **527**, 212 (2015).
[23] N. Nagaosa, J. Sinova, S. Onoda, A. H. MacDonald, and N. P. Ong, Rev. Mod. Phys. **82**, 1539 (2010).
[24] M. Kimata, H. Chen, K. Kondou, S. Sugimoto, P. K. Muduli, M. Ikhlas, Y. Omori, T. Tomita, A. H. MacDonald, S. Nakatsuji, and Y. Otani, Nature (London) **565**, 627 (2019).
[25] M. Ikhlas, T. Tomita, T. Koretsune, M.-T. Suzuki, D. Nishio-Hamane, R. Arita, Y. Otani, and S. Nakatsuji, Nat. Phys. **13**, 1085 (2017).
[26] T. Higo, H. Man, D. B. Gopman, L. Wu, T. Koretsune, O. M. J. van't Erve, Y. P. Kabanov, D. Rees, Y. Li, M.-T. Suzuki, S. Patankar, M. Ikhlas, C. L. Chien, R. Arita, R. D. Shull, J. Orenstein, and S. Nakatsuji, Nat. Photonics **12**, 73 (2018).
[27] K. Kuroda, T. Tomita, M.-T. Suzuki, C. Bareille, A. A. Nugroho, P. Goswami, M. Ochi, M. Ikhlas, M. Nakayama, S. Akebi, R. Noguchi, R. Ishii, N. Inami, K. Ono, H. Kumigashira, A. Varykhalov, T. Muro, T. Koretsune, R. Arita, S. Shin, T. Kondo, and S. Nakatsuji, Nat. Mater. **16**, 1090 (2017).
[28] H. Yang, Y. Sun, Y. Zhang, W.-J. Shi, S. S. P. Parkin, and B. Yan, New J. Phys. **19**, 015008 (2017).
[29] Y. Song, Y. Hao, S. Wang, J. Zhang, Q. Huang, X. Xing, and J. Chen, Phys. Rev. B **101**, 144422 (2020).
[30] H. Ohmori, S. Tomiyoshi, H. Yamauchi, and H. Yamamoto, J. Magn. Magn. Mater. **70**, 249 (1987).
[31] E. Krén and J. Paitz, G. Zimmer, and É. Zsoldos, Phys. B **80**, 226 (1975).
[32] W. J. Feng, D. Li, W. J. Ren, Y. B. Li, W. F. Li, J. Li, Y. Q. Zhang, and Z. D. Zhang, Phys. Rev. B **73**, 205105 (2006).
[33] S. Tomiyoshi, S. Abe, Y. Yamaguchi, H. Yamauchi, and H. Yamamoto, J. Magn. Magn. Mater. **54**, 1001 (1986).
[34] P. Brown, V. Nunez, F. Tasset, J. Forsyth, and P. Radhakrishna, J. Phys.: Condens. Matter **2**, 9409 (1990).
[35] S. Tomiyoshi, J. Phys. Soc. Jpn. **51**, 803 (1982).
[36] S. Tomiyoshi and Y. Yamaguchi, J. Phys. Soc. Jpn. **51**, 2478 (1982).
[37] G. J. Zimmer and E. Krén, *Magnetism and Magnetics Materials — 1971 Parts 1 and 2*, edited by C. D. Graham and J. J. Rhyne, AIP Conf. Proc. No. 5 (AIP, New York, 1972), p. 513.
[38] Y. Zhang, Y. Sun, H. Yang, J. Železný, S. P. P. Parkin, C. Felser, and B. Yan, Phys. Rev. B **95**, 075128 (2017).
[39] Y.-Y. Wang, S. Xu, L.-L. Sun, and T.-L. Xia, Phys. Rev. Mater. **2**, 021201(R) (2018).
[40] Z. Qiu, C. Le, Z. Liao, B. Xu, R. Yang, J. Hu, Y. Dai, and X. Qiu, Phys. Rev. B **100**, 125136 (2019).
[41] R. Kealhofer, S. Jang, S. M. Griffin, C. John, K. A. Benavides, S. Doyle, T. Helm, P. J. W. Moll, J. B. Neaton, J. Y. Chan, J. D. Denlinger, and J. G. Analytis, Phys. Rev. B **97**, 045109 (2018).
[42] K. Haule, C.-H. Yee, and K. Kim, Phys. Rev. B **81**, 195107 (2010).
[43] P. Blaha, K. Schwarz, G. Madsen, D. Kvasnicka, and J. Luitz, *WIEN2K, An Augmented Plane Wave+Local Orbitals Program for Calculating Crystal Properties* (Karlheinz Schwarz, Techn. Universität Wien, Austria, 2001).
[44] J. P. Perdew, K. Burke, and M. Ernzerhof, Phys. Rev. Lett. **77**, 3865 (1996).
[45] P. Werner, A. Comanac, L. de' Medici, M. Troyer, and A. J. Millis, Phys. Rev. Lett. **97**, 076405 (2006).
[46] K. Haule, Phys. Rev. B **75**, 155113 (2007).
[47] G. Kresse and J. Furthmüller, Phys. Rev. B **54**, 11169 (1996).

[48] See Supplemental Material at http://link.aps.org/supplemental/10.1103/PhysRevB.106.205103 for calculated electronic band structures with different combinations of U and J_H (Fig. S1), comparison between experimentally measured and calculated ARPES obtained with different Hund's coupling parameters (Fig. S2), and DFT calculated band structure in the nonmagnetic state without spin-orbit coupling (Fig. S3).

[49] F. Hardy, A. E. Böhmer, D. Aoki, P. Burger, T. Wolf, P. Schweiss, R. Heid, P. Adelmann, Y. X. Yao, G. Kotliar, J. Schmalian, and C. Meingast, Phys. Rev. Lett. **111**, 027002 (2013).

[50] Z. P. Yin, K. Haule, and G. Kotliar, Phys. Rev. B **86**, 195141 (2012).

[51] J. Kübler and C. Felser, Europhys. Lett. **120**, 47002 (2017).